A Study of Coaxial Rotor Performance and Flow Field Characteristics

Natasha L. Barbely
Aerospace Engineer
NASA Ames Research Center
Moffett Field, California , USA

Narayanan M. Komerath
Professor
Georgia Institute of Technology
Atlanta, Georgia, USA

Luke A. Novak
Aerospace Engineer
Sukra Helitek, Inc.
Ames, Iowa, USA

ABSTRACT

As a precursor to studying the acoustics of a coaxial rotor system, the aerodynamics and flow field of a coaxial rotor were simulated to better understand the interaction between the two rotors. RotUNS, an unsteady Navier-Stokes solver that uses a simplified blade aerodynamics model, was used to predict coaxial rotor performance in hover and forward flight. RotUNS steady hover calculations showed improved performance compared to blade element momentum theory. Prior to examining the complex 3D flow field of a coaxial rotor in detail, two airfoils traveling in opposite directions with a vertical separation distance equivalent to the separation between the upper and lower rotor of the coaxial system were simulated. The pressure field generated by the two airfoils aided our interpretation of the more complex coaxial rotor system flow field. The pressure fields above, between, and below the coaxial rotor system were then examined for different azimuth positions of the upper and lower rotor blades.

NOTATION

B_1	single rotor blade 1
B_2	single rotor blade 2
c	chord (ft)
C_d	coefficient of drag
C_l	coefficient of lift
C_P	rotor power coefficient
C_T	rotor thrust coefficient
D	rotor diameter (ft)
$L1$	lower rotor blade 1
$L2$	lower rotor blade 2
N_b	number of blades (per rotor)
Q	torque (lbs-ft/s)
R	rotor radius (ft)
r/R	dimensionless radial position
T_U	upper rotor thrust (lbs)
T_L	lower rotor thrust (lbs)
$U1$	upper rotor blade 1
$U2$	upper rotor blade 2
V	forward flight velocity (ft/sec)
Z	vertical distance between rotors (ft)
α_S	pitch angle (deg), negative pitch down
κ_{int}	coaxial rotor induced power interference factor
μ	advance ratio (V/tip speed)
σ	rotor solidity
θ_S	single rotor collective pitch angle (deg)
θ_L	lower rotor collective pitch angle (deg)
θ_U	upper rotor collective pitch angle (deg)
θ_{1cU}	upper rotor lateral cyclic pitch (deg)
θ_{1cL}	lower rotor lateral cyclic pitch (deg)
θ_{1sU}	upper rotor longitudinal cyclic pitch (deg)
θ_{1sL}	lower rotor longitudinal cyclic pitch (deg)

Presented at the 2016 AHS Technical Meeting on Aeromechanics Design for Vertical Lift, Fisherman's Wharf, San Francisco, CA January 20–22, 2016.

INTRODUCTION

Coaxial rotorcraft are finding increasing use in civil and military applications, as well as in the small unmanned aerial vehicles (UAVs) market. As with all rotorcraft, the rotor noise generated by a coaxial rotor system must be mitigated to minimize impact to the community. Unlike single-main rotor or tiltrotor configurations, however, there are only limited studies, analytical or experimental, on coaxial rotor noise (Refs. 1–6). Studies on coaxial rotor performance are highlighted below.

Coleman (Ref. 7) provides a thorough summary of experimental and analytical studies of coaxial rotors through 1997. In the U. S., the first documented coaxial rotor test was a hover test by Taylor in 1950 (Ref. 8) in the full-scale wind tunnel at NASA Langley Research Center. The coaxial rotor consisted of two 20-in diameter rotors, with two blades per rotor. The test objective was to visualize the flow through several (single, coaxial, tandem) rotor configurations with and without a ground plane present.

A surprisingly small number of coaxial rotor hover experiments have been performed since the Taylor test, with the work by Ramasamy (Ref. 9) being the most comprehensive. Ramasamy (Ref. 9) measured the performance of single, coaxial, tandem, and tiltrotor configurations using untwisted and twisted blade sets. The coaxial rotor system comprised two independent test rigs allowing performance measurements of the upper and lower rotor separately. Ramasamy provided a convenient summary of coaxial rotor hover performance measurements prior to 2013, including those surveyed

by Coleman. More recently, Cameron et al. (Ref. 10) measured the performance of a single rotor and coaxial rotor system using an 80-in diameter rotor with untwisted blades. Hub loads and blade deformation were also measured.

Coaxial rotor measurements in forward flight are scarcer compared to hover. Since 1997, the data from the Sikorsky X2 (Ref. 11) flight test joins the handful of forward flight measurements included in the Coleman survey.

Analysis of coaxial rotor systems has progressed over the last decade thanks to improved modeling capabilities. Leishman and Ananthan (Ref. 12) developed a Blade Element Momentum Theory (BEMT) model for coaxial rotors in hover and axial flight to design an optimum coaxial rotor for hover. Leishman and Ananthan (Ref. 12) used the Harrington data (Ref. 13) to validate the BEMT model. Using momentum theory and the Harrington data, Leishman and Syal (Ref. 14) developed figure of merit expressions for a coaxial rotor for four different operating conditions; the results are used in the present paper. Ho et al. (Ref. 15) summarize some of the more recent validation studies of coaxial rotors. Analysis validations have relied primarily on the Harrington (Ref. 13) and Dingeldein (Ref. 16) large-scale coaxial rotor data. Though the Ramasamy data are for an approximately 4.3-ft diameter coaxial rotor system, the individual rotor performance measurements are valuable for analysis validation. Ho et al. (Ref. 15) used RCAS (a comprehensive rotorcraft analysis) to model the rotors used by Harrington and Ramasamy to compute coaxial rotor performance in hover and forward flight. Table 1 lists the validation studies discussed by Ho et al. (Ref. 15), including the configurations modeled and the dataset used for validation. In addition, Table 1 includes work not covered by Ho: Kim and Brown (Refs. 3,4,17,18), Juhasz et al. (Ref. 19), Schmaus and Chopra (Ref. 20), and Singh and Kang (Ref. 21).

Kim and Brown (Refs. 3, 4, 17, 18) exercised their Vorticity Transport Model (VTM) analysis, and also predicted maneuverability performance of a lift-offset rotor using Harrington (Ref. 13) and Dingeldein (Ref. 16) data for validation and design. Kim and Brown (Refs. 3, 4) are one the few efforts to study coaxial rotor noise.

Juhasz et al. (Ref. 19) applied three aerodynamic prediction models to McAlister et al. (Ref. 22) model-scale coaxial rotor in hover. The three models includes BEMT, a free-vortex wake model and CFD using OVERFLOW2. A combination of the three methodologies was found to be the best method to analyze the aerodynamics, though dependent on the level of detail desired.

Schmaus and Chopra (Ref. 20) developed a comprehensive analysis for a coaxial rotor for high advance ratios, using the code UMARC. The experimental rotor data from the University of Texas at Austin (Ref. 10) along with Harrington rotor 1 (Ref. 13) and the XH-59A (Ref. 23) are used for validation. Using the University of Texas rotor (Ref. 10), the flight envelope for high advance ratios is defined for anticipated experimental tests.

Singh and Kang (Ref. 21) performed computational simulations using a loose coupled CFD(Helios)/CSD(RCAS) approach using a micro-scale coaxial rotor in hover from the University of Texas (Ref. 10). Results revealed that due to the interference between the upper and lower rotor, the two rotors need to be modeled using a CSD solver in order to have a robust trim convergence.

In efforts to continue the ongoing research of coaxial rotors, the performance and flow field characteristics are explored in this paper. This current work uses the hybrid-CFD analysis tool RotUNS for hover and forward flight performance predictions to compare against Harrington (Ref. 13) and Dingeldein (Ref. 16) data. The effect of the relative position of the upper and lower rotor blades on the flow field pressures near the rotor blades, which are important for acoustics, is studied. This exploration of the physics of coaxial aerodynamics and adds to the computational work of Table 1.

Rotor Unstructured Navier-Stokes (RotUNS)

The Rotor Unstructured Navier-Stokes (RotUNS) analysis was used to explore coaxial rotor aerodynamics for this paper.

RotUNS operates within the RotCFD Integrated Design Environment (IDE) (Refs. 24, 25). RotCFD offers a bridge between comprehensive rotorcraft analysis and CFD analysis. RotUNS is one of several flow solvers within RotCFD, which also includes a geometry module, a semi-automated grid generation module, a rotor module, and a flow visualization and analysis module, all integrated in one environment. Operating within the RotCFD IDE, grid generation and problem set-up are quickly executed, facilitating parametric sweeps of rotor conditions and problem geometry. RotCFD balances ease of use and practical resource constraints with accurate physical representation of the global flow field.

RotUNS uses 3D incompressible Reynolds Averaged Navier-Stokes (RANS) equations and an unstructured grid in the far field (Refs. 24, 25). Two options are available to model the rotor: actuator disk and discrete blade. Both options rely on user-provided tables of two-dimensional airfoil coefficients for a range of angle-of-attack and Mach number. Using the computed velocity field and blade element momentum theory, the local angle of attack and the Mach number at each blade element section is computed and the aerodynamic coefficients are retrieved from the airfoil tables. For the discrete blade model of the rotor, the section forces and moments are then converted to source terms that are added to the momentum equations at grid points where the blade intersects.

Unlike the disk rotor model, the discrete blade model comprises an individual lifting line representing each blade. The lifting-line changes location with time. In order to calculate the time-varying rotor sources, the instantaneous location of each rotor blade is found, followed by the calculation of the time-accurate rotor force that the blades exert on specific regions of the flow. Each rotor blade is divided into about 100

source locations and the azimuth position of the blade is assumed to vary linearly with time. At each time step, the starting and ending azimuthal position of a rotor blade are computed and used to find the coordinates of the blade sections and the intersections with the grid cells. The rotor sources are computed similar to the disk model and added to the momentum equations for the grid cell. The solution is then advanced in time.

All performance predictions in this paper were calculated using the disk (steady) rotor model of RotUNS. The pressure fields were generated using the lifting-line (unsteady) rotor model to assess the effect of individual blades.

HARRINGTON SINGLE (HS1) AND COAXIAL ROTOR 1 (HC1)

The performance and aerodynamics of the Harrington single rotor 1 (HS1) and coaxial rotor 1 (HC1) were predicted using RotUNS with the rotor disk model. Although the experimental data for hover (Ref. 13) and forward flight (Ref. 16) are available, rotor control setting information is not. Unsteady calculations are explored to understand qualitatively the characteristics of the HS1 and HC1 flow field.

Geometry description

The geometry for HS1/HC1 is provided in Table 2; blade planform as modeled in RotUNS is shown in Fig. 1. The difference in the blade geometry for the HS1 and HC1 Harrington experiment (Ref. 13) and RotUNS is that the Harrington blades have a continuously varying non-linear distribution of airfoil thickness. At this time, RotUNS does not allow a continuously varying airfoil thickness distribution, so nine NACA airfoils with varying thickness ratios are used to simulate the blade for HS1 and HC1. NACA airfoil tables are kept constant between each radial distance station as shown in Fig. 1, while the C81 tables are interpolated for changing r/R location for determining c_l and c_d. Airfoil C81 tables were generated using a 2D Navier-Stokes solver and are used for all RotUNS and BEMT calculations.

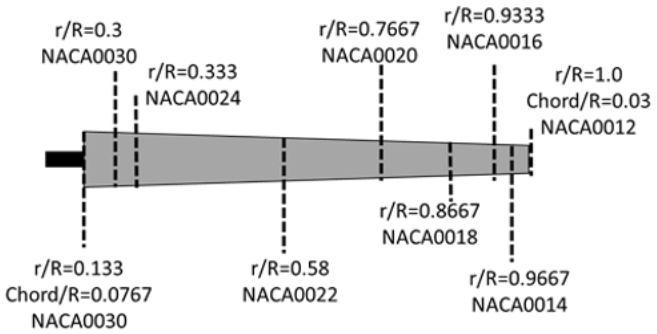

Fig. 1. HS1/HC1 blade planform geometry as modeled in RotUNS.

Harrington single rotor 1 (HS1) hover performance

Figure 2 shows RotUNS and BEMT hover calculations compared with measurements by Harrington (Ref. 13) for the HS1 rotor for a collective pitch range from 1.5° to 9°. The BEMT predictions are based on Leishman's single-rotor blade element model (Ref. 12). In Fig. 2, BEMT is under-predicting thrust for high values of power due to BEMT assumptions (Ref. 26). The RotUNS calculations compare well with the Harrington (Ref. 13) data.

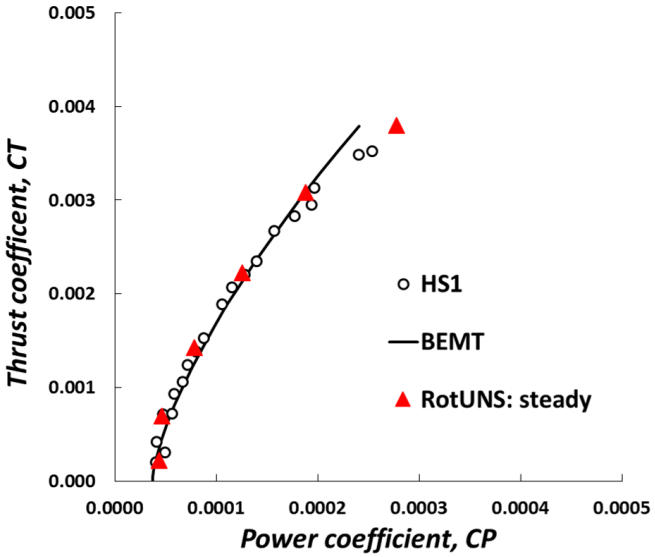

Fig. 2. Performance of HS1 (Ref. 13) in hover compared with BEMT and RotUNS steady calculations.

Harrington coaxial rotor 1 (HC1) hover performance

Figure 3 compares performance measurements (Ref. 13) with predictions from RotUNS, RotUNS: GA, and the BEMT analysis for the HC1 system. RotUNS offers a Grid Adaption (GA) option. Grid adaption, based on vorticity, was used for a few of the cases in anticipation of the complex interaction between the upper and lower rotor. The use of GA redefines and refines the mesh over time, allowing flow features to be captured with greater fidelity. Comparing Fig. 2 and Fig. 3, for HS1 at zero thrust BEMT calculations are large compared to experiment and RotUNS calculations due to the BEMT input of κ_{int} being too small and minimum c_d to large (Ref. 27). The BEMT calculations for HC1 are closer to experiment and RotUNS calculations compared to HS1 due to appropriate assumptions made (Ref. 12).

Since RotUNS does not yet include a trim procedure, collective settings for the upper and lower rotor were determined through an iterative process to achieve a torque-balanced solution. As shown in Table 3, torque balance was achieved for most of the cases by increasing the collective of the lower rotor by 0.2°compared to the upper rotor. Table 3 provides the percent torque difference between the upper and lower rotors;

for the present work, a difference of $< 1\%$ was considered a balanced system. The thrust for the coaxial lower rotor is less than the coaxial upper rotor which is due to the increased inflow seen by the lower rotor from the upper rotor (Ref. 12).

The BEMT uses the same geometry assumptions as the RotUNS calculations while using a coaxial interference-induced power factor from Leishman's Case 4a (Refs. 12, 14). Leishman's Case 4a assumes that the rotors have balanced torque with the lower rotor operating in the slipstream of the upper rotor.

RotUNS run with grid adaption shows an improvement at higher collective settings, but little or no change at lower thrust. Differences between Harrington's (Ref. 13) data and computational simulations can be due to blade modeling. The actual Harrington's HS1 and HC1 had smooth airfoil (thickness to chord) transitions, unlike the geometry that was used by RotUNS and BEMT. Another justification for the difference between experimental and RotUNS is that the blades are modeled as momentum sources, not as actual blades.

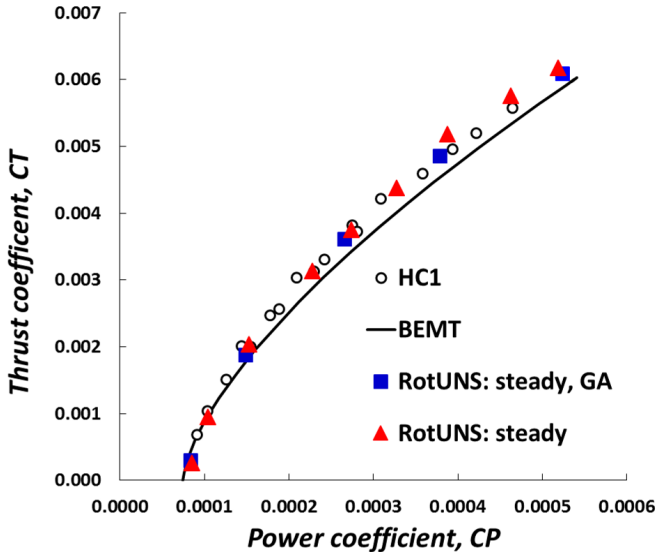

Fig. 3. Performance of HC1 (Ref. 13) in hover compared with momentum theory, BEMT and RotUNS steady calculations.

Rotor separation distance variation: The performance of HC1 was explored from 0.05 to 1.5 Z/D, where Z is the vertical distance between the two rotors. Figure 4 reveals that as separation distance increases the ratio between thrust of the lower rotor (T_L) and upper rotor (T_U) decreases, for balanced torque and constant total thrust coefficient, eventually becoming independent of separation distance. A similar trend is seen for both the RotUNS calculations and measurements by Ramasamy (Ref. 9) for two different total thrust coefficients (and blade geometry) leading confidence in RotUNS prediction capability.

As previously mentioned, the RotUNS rotor collective pitch settings were determined through an iterative process to achieve a torque-balanced solution; the percent difference in torque is seen in Table 4.

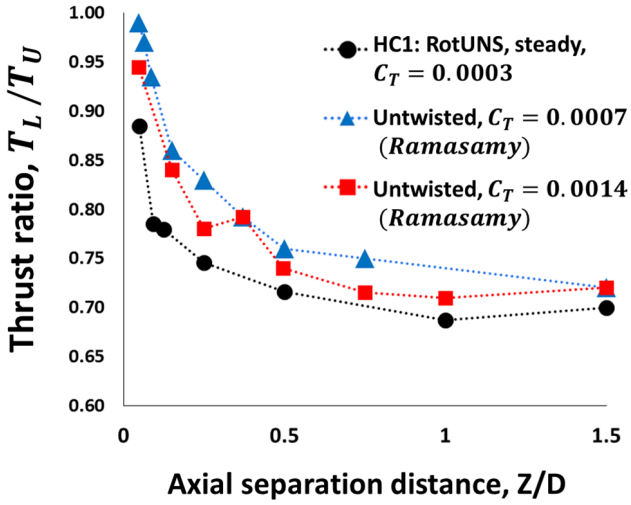

Fig. 4. Thrust ratio verses rotor separation distance in hover comparing HC1 RotUNS steady calculations and Ramasamy's (Ref. 9) experimental data for untwisted blades.

Wake geometry for a hovering coaxial rotor: Vortex diffusion is a critical issue with all computational simulations of rotor wakes. Using resolution enhancements in the grid, vortices can be preserved longer. Kim and Brown (Ref. 17) conducted a similar computational investigation using the Vorticity Transport Model (VTM) developed by Brown while coupled with a lifting-line representation of the blade. Without the use of grid adaption in RotUNS, the tip vortices are not discernible after approximately 120 degrees of vortex age (see Fig. 5) though the calculation represents 50 rotor revolutions. RotUNS was next run with grid adaption (GA) for a small set of thrust/collective settings. The grid was automatically refined in areas of high vorticity and coarsened in areas of low vorticity (Fig. 6). The RotUNS GA resulted in a slightly better agreement with experimental data compared to the RotUNS baseline grid results shown in Fig. 3. Figure 7 shows the effect of GA for HC1; vorticity is captured further below the rotor with GA.

The use of GA resulted in a slightly better agreement between rotor performance predictions and experimental data as compared to the RotUNS baseline grid results shown Fig. 3. Not all of the GA cases are as well torque-balanced as the baseline grid cases, however. In summary, the baseline grid is sufficient for performance predictions but a detailed study of wake interactions will require grid adaption or a finer baseline grid.

Forward flight validation

For forward flight predictions, trim settings for the HC1 rotor were required. Here, RotUNS relied on trim control solutions

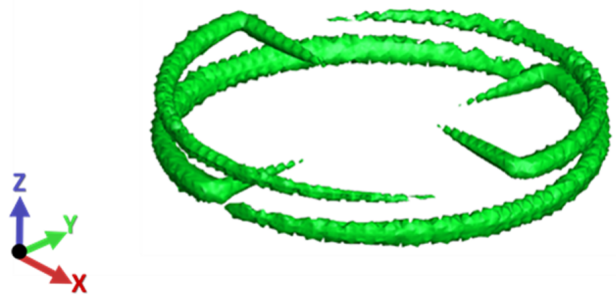

Fig. 5. Wake geometry for HC1 (Q-criterion = 0.001 iso-surfaces after 50 revolutions) RotUNS unsteady calculations.

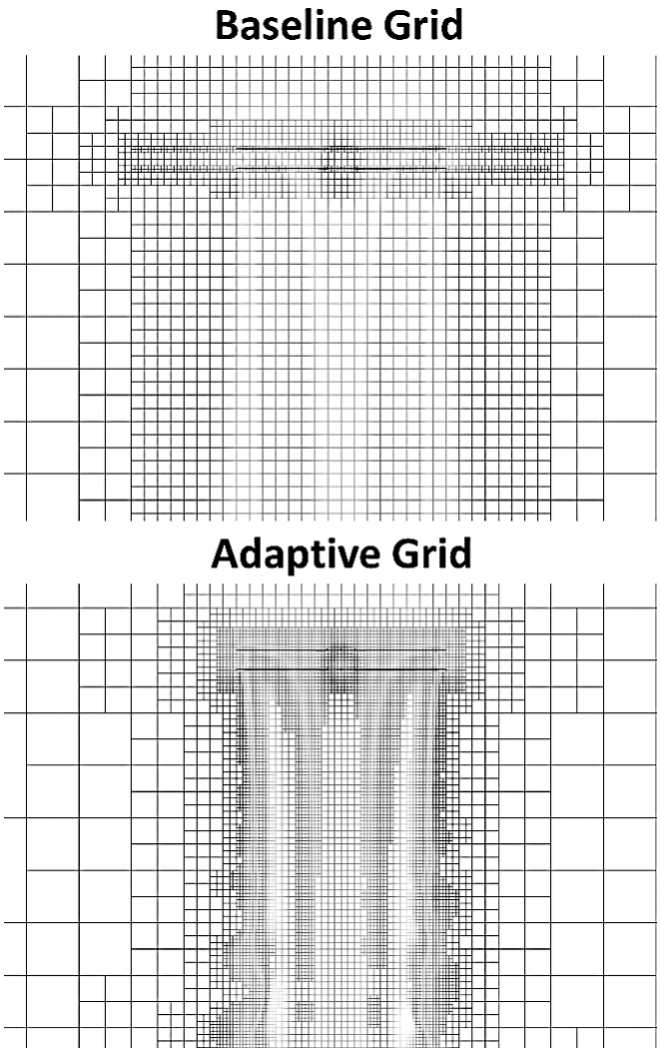

Fig. 6. Comparison of baseline and adaptive wake grid ($\theta_U = \theta_L = 10^\circ$) for HC1 RotUNS steady calculations.

provided by CAMRAD II (Ref. 28); the settings are provided in Table 5.

CAMRAD II (Ref. 29) is a rotorcraft analysis tool that includes a combination of advanced technologies, including

Fig. 7. Comparison of baseline and adaptive grid wake geometry ($\theta_U = \theta_L = 10^\circ$) for HC1 (Vorticity iso-surface) RotUNS steady calculations.

multibody dynamics, nonlinear finite elements, and rotorcraft aerodynamics. The rotor structural-dynamics model is based on beam theory. The rotor-aerodynamics model is based on second-order lifting-line theory (steady two-dimensional airfoil characteristics plus vortex wake), with unsteady aerodynamic forces from thin airfoil theory, and corrections for yawed flow and swept blades.

In CAMRAD II, the rotors were trimmed to zero flapping while adjusting the collective pitch and the lateral and longitudinal cyclic of each rotor with a fixed shaft pitch angle. The HC1 rotor blades were modeled using 17 aerodynamic panels in CAMRAD II, with the panel width ranging from 8% R at the root to 3% R at the tip. Unlike the RotUNS blade model, which used the airfoil distribution shown in Fig. 1, the CAMRAD II blade model used a constant NACA0012 airfoil section. Additional details of the HC1 CAMRAD II model are available from (Ref. 28).

Figure 8 shows the measured forward flight performance of HC1 (Ref. 16) compared to CAMRAD II and RotUNS cal-

culations. Though the CAMRAD II calculations show better correlation with experimental data compared to the RotUNS calculations, recall that the two analyses use very different airfoil distributions with RotUNS providing a airfoil thickness distribution that is more representative of the HC1 rotor. For each airfoil, a 2D Navier-Stokes analysis was used to generate airfoil tables that were read by RotUNS. An increment to the section profile drag was added as part of the shaft power calculation in CAMRAD II. Since the control inputs used in RotUNS are not directly coupled with the resulting aerodynamic solution within RotUNS but rather the aerodynamic model within CAMRAD II, the resulting differences in the required shaft power between CAMRAD II and RotUNS are not unexpected. A natively coupled trim capability within RotUNS is expected to improve the RotUNS calculations. The difference in torque for the upper and lower rotor for each advance ratio and collective setting is provided in Table 6.

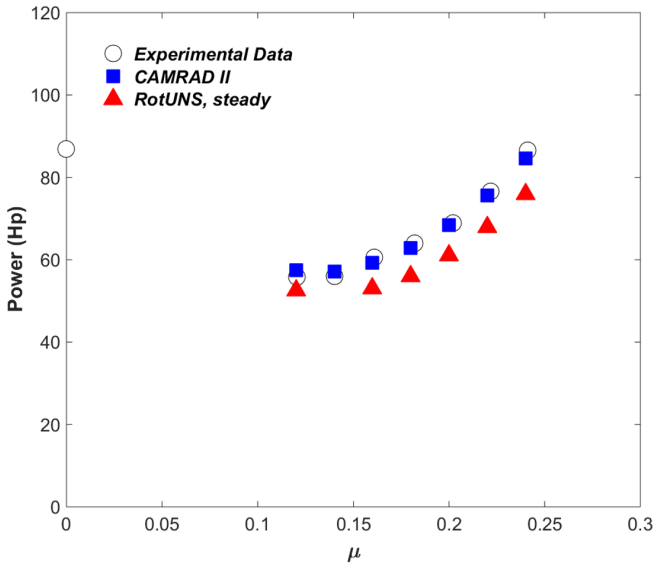

Fig. 8. Performance of HC1 (Ref. 16) in forward flight compared with CAMRAD II and RotUNS steady calculations

.

DETAILED ANALYSIS OF FLOW FIELD IN HOVER

The aerodynamics of coaxial rotors is quite complex since each rotor operates in the induced flow field produced by the other rotor. To simplify this 3D problem, a 2D unsteady simulation of two airfoils traveling in opposite directions was performed using OVERFLOW. The vertical separation distance between the airfoils is equivalent to the separation distance between the HC1 rotors. The 2D simulation aids in understanding the behavior of the flow field. Next, RotUNS 3D simulations were analyzed for the HS1 and HC1 rotors. Unlike a 2D simulation, the exact time of blade overlap of two counter-rotating rotors with more than one blade each requires careful accounting. Therefore, a code was developed to predict the time and location of blade overlap.

The discrete blade rotor model was used in the RotUNS simulations to generate results in the following section.

2D airfoils crossing over time

Analysis begins with an OVERFLOW (Ref. 30) simulation of two airfoils traveling in opposite directions. The same geometry(NACA0020) and parameters for the HC1 at r/R=0.8 was used to simulate two airfoils moving past each other at an angle of attack of 7° and V=425 ft/s (Mach 0.38) was used.

OVERFLOW (Ref. 30), developed by NASA, is a compressible Reynolds Averaged Navier-Stokes CFD analysis that can use overset grids. Due to the differences between OVERFLOW and RotUNS in terms of modeling and solver methodologies, differences are expected for this flow condition, but the qualitative behavior of the flow should be similar.

Figure 9 depicts the airfoil locations before, during, and after time of overlap. The pressure field predicted by OVERFLOW is shown Fig. 10 when the airfoils cross and after the upper airfoil has departed. Figure 11 shows time histories of the absolute pressure at mid-chord slightly above and below the upper and lower airfoil (see colored circles in Fig. 9). Figure 9a) is the pressure below the upper and lower rotor while Figure 9b) is the pressure above the upper and lower rotor; the figures use different absolute pressure scales to better visualize the flow. The absolute pressure above the upper and lower airfoil is lower compared to the absolute pressure beneath the upper and lower airfoil which explains the fundamental reason that lift is generated over an airfoil (Ref. 31).

As the two airfoils come closer to each other, the upper airfoil sees an overall decrease in absolute pressure, while the lower airfoil sees the opposite with an overall increase in absolute pressure. The upper airfoil enters a region of low pressure due to the pressure above the lower airfoil (low pressure) causing an overall decrease in absolute pressure. The lower airfoil enters a region of high pressure due to the pressure below the upper rotor (high pressure) causing an overall increase in absolute pressure.

Pressure distribution above and below rotor

The pressure field of two airfoils analyzed in the previous section provides an understanding for a 3D pressure field of two contra-rotating rotors. Before progressing to the 3D field, a MATLAB (Ref. 32) code was created to identify the time and azimuth at which a reference blade of the upper (or lower) rotor crosses a lower (or upper) rotor blade (see Fig. 12) of a coaxial rotor. The code aids in pinpointing locations of interests of pressure and velocity fields between or at the rotors.

The code outputs the quantitative results and graphically displays the blades in motion. When an upper and lower rotor blade cross, a marker is placed along the azimuth at the crossing point. The upper and lower rotors can have different parameters including: RPM, number of blades, blade phase

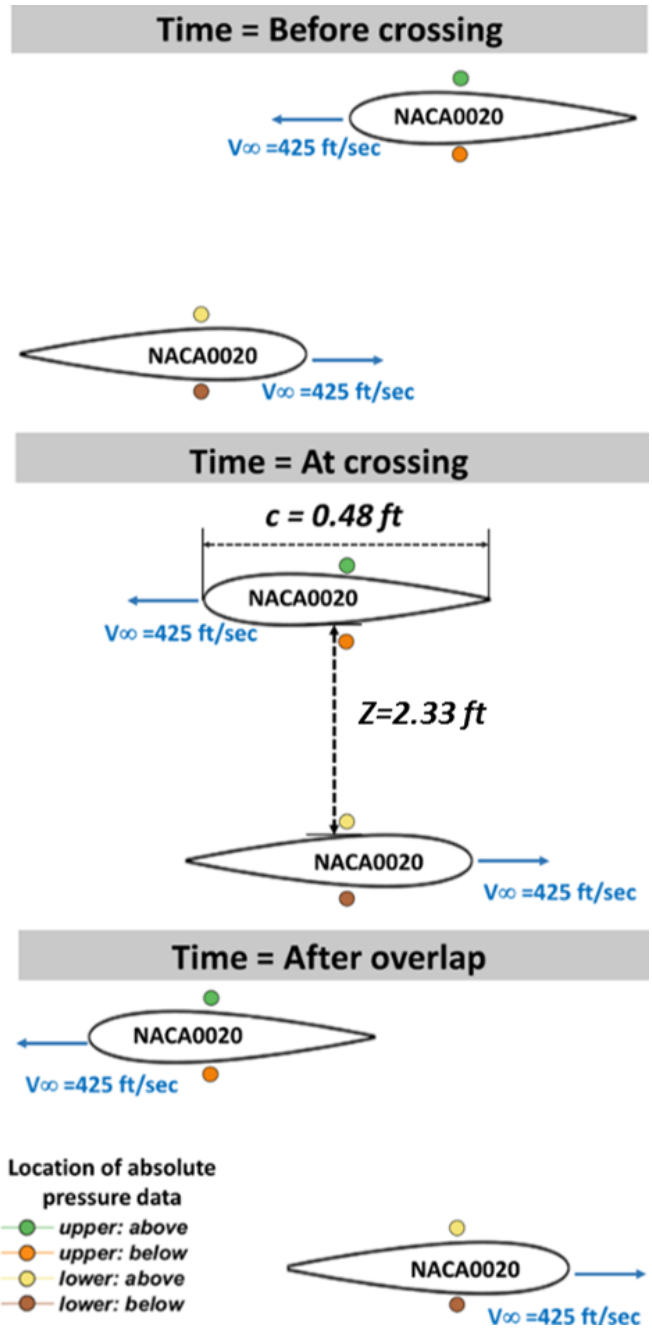

Fig. 9. 2D OVERFLOW simulation model of two airfoils before, at and after crossing.

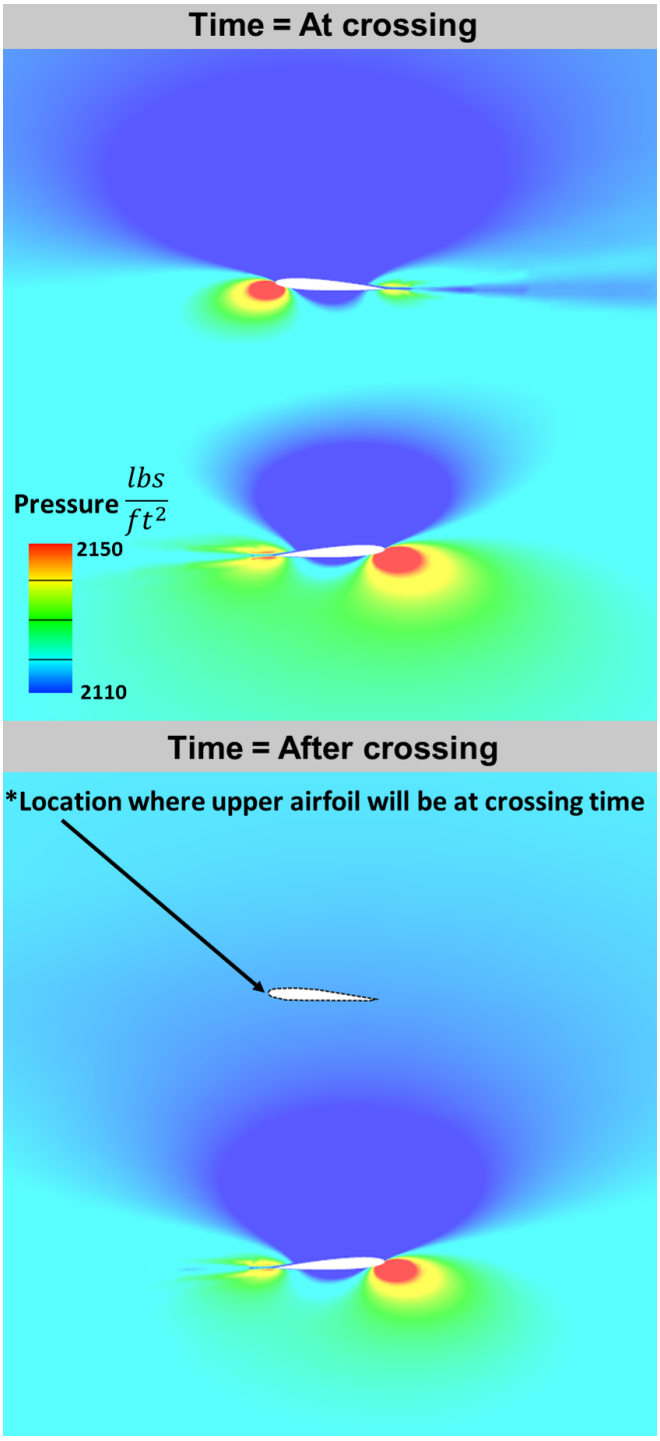

Fig. 10. 2D OVERFLOW calculations for the flow field pressure distribution of two airfoils crossing and after crossing.

location, reference blade of either rotor, radius, and chord. The reference blade is identified by first selecting the upper or lower rotor and then selecting the blade. A blade crossing is recorded when a reference blade and a blade from the other rotor overlap. For a coaxial rotor with two blades on the upper rotor and two blades on the lower rotor (rotating in opposite directions), using blade 2 of the lower rotor (L2) as the reference blade with an initial starting location at 270° azimuth, the code predicted 4 overlaps of the reference blade in one rotor revolution. Overlaps with L2 occur in the following order for one revolution: U1 (upper rotor blade 1) at 225°, U2 (upper rotor blade 2) at 135°, U1 at 45° and U2 at 315°.

The pressure above and below a hovering rotor was analyzed using the discrete-blade option of RotUNS. A single rotor was analyzed first and then a coaxial rotor. The Harrington rotor 1 was simulated with all rotors (single, upper/lower rotor) set to a collective pitch of 7°.

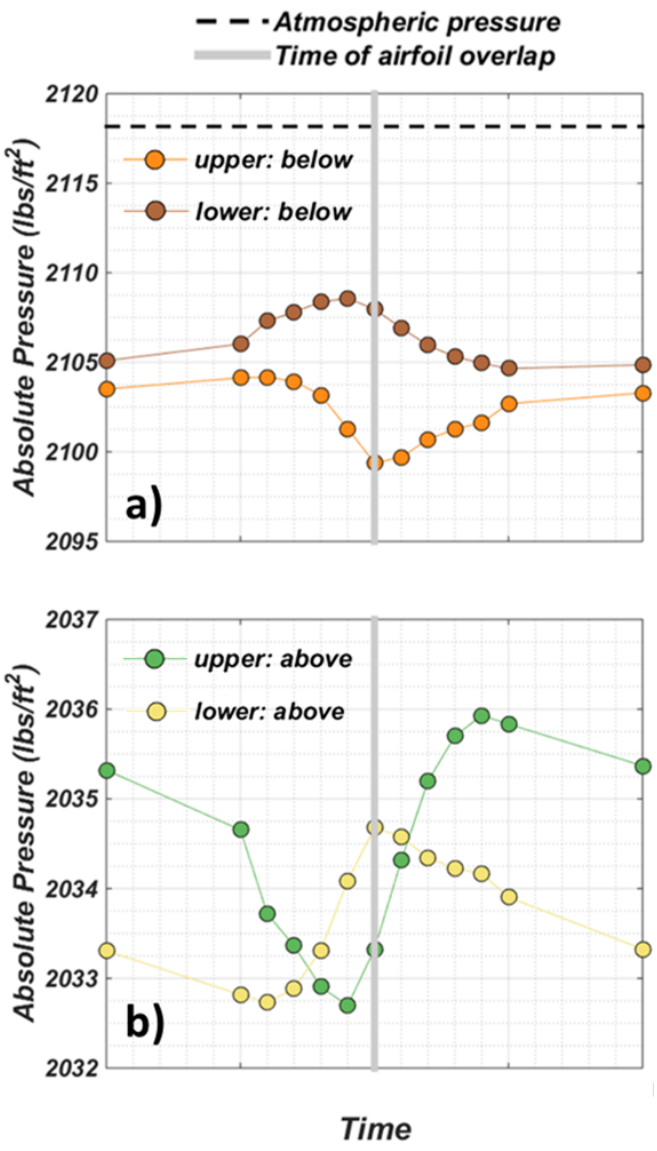

Fig. 11. Pressure time histories for: a) slightly below each airfoil and b) slightly above each airfoil.

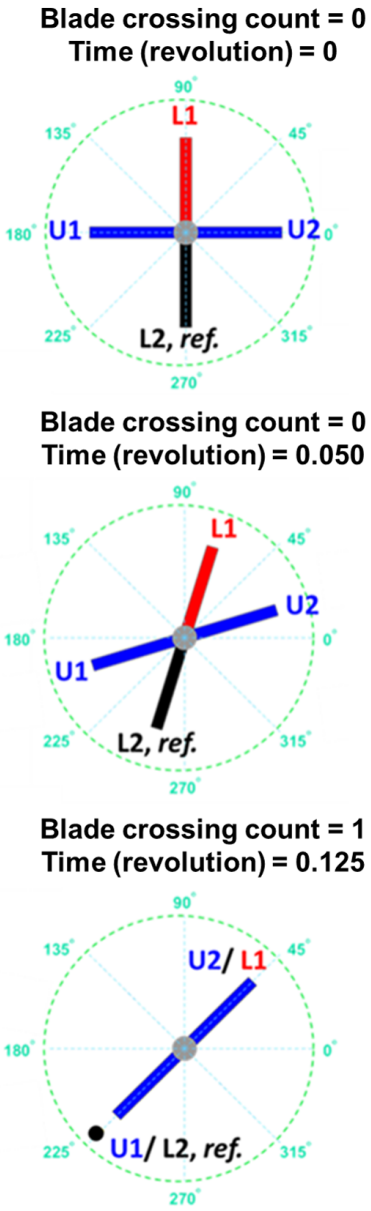

Fig. 12. Blade overlap time prediction MATLAB code visual output of 2 bladed coaxial rotor.

The pressures below and above the rotor(s) are shown in Figs. 13-17, which represent the absolute pressure normal to the surface at the closest flow field grid point for HS1 and HC1. The figures simply illustrate the pressure change (lower or higher) as blades from the upper and lower rotors pass in opposite directions.

The absolute pressure below and above a single isolated rotor is shown in Fig. 13 when the blades are at 0° (B1) and 180° (B2). A low pressure is evident above both blades and a high pressure below the blades, providing a positive upward thrust. Figure 14 shows time histories of pressure just above and below blade B1 at r/R=0.85 in the rotating frame; the pressure remains essentially constant throughout one revolution.

When a second rotor is introduced, the flow field becomes complex, as shown in Figs. 15 -17.

The absolute pressure below and above each rotor of HC1 is presented in Figs. 15 -16. In both figures, the pressure above the upper rotor is the top-left figure and the pressure below the upper rotor is the bottom-left figure. The pressures above and below the lower rotor are represented by the upper- and lower-right figures, respectively.

Figure 15 shows an instance when the blades of the upper and lower rotor are not overlapped. The upper rotor blades are at 0° (U1) and 180° (U2) and the lower rotor blades are at 90° (L1) and 270° (L2). The presence of the lower rotor is seen at 90° and 270° in the upper rotor pressure above and below contour, which reveals the above pressure from the lower rotor. The same is also seen for the lower rotor pressure above and below, where the upper rotor pressure below is seen at 0° and 180°. For both upper and lower rotors, a low pressure is seen at the location of the blades above and high pressure

below the rotors, giving rise to a positive upward thrust.

Figure 16 shows an instance when the upper and lower blades are overlapped at 45° (U1) and 135° (U2) for the upper rotor and 45° (L1) and 135° (L2) for the lower rotor. In comparison to Fig. 15, when the blades are not overlapped, a difference in pressure below and above is seen. When the blades are overlapped, the pressure above the upper rotor decreases. A decrease in pressure below is also seen for the upper rotor. The opposite is seen for the lower rotor, where the pressure above and below have an increase in pressure.

The time histories of the pressure above and below the upper and lower rotor blades at an r/R of approximately 0.85 in the rotating frame are presented in Fig. 17. The gray vertical line indicates the time of blade overlap. For both the upper and lower rotors, a change in pressure is seen at the time of blade overlap. Blade 2 (U2) of the upper rotor experiences an overall decrease in pressure due to the low-pressure field generated from Blade 1 (L1) of the lower rotor. Conversely, L1 experiences an increase in pressure due to the high-pressure field of U2. Comparing Fig. 17 to Fig. 14, an aerodynamic interaction is seen between the upper and lower rotor in the coaxial rotor system, unlike the single rotor.

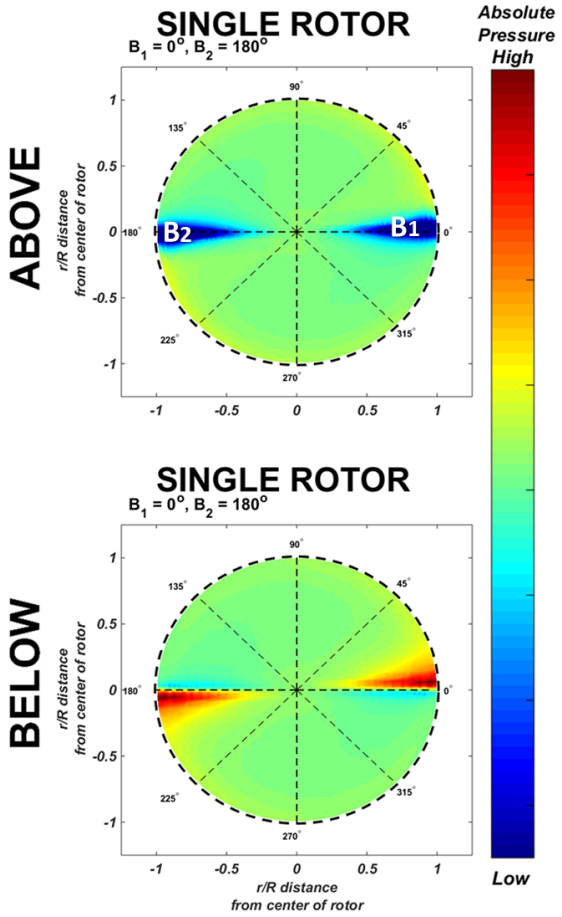

Fig. 13. HS1 absolute pressure below and above rotor RotUNS unsteady calculations.

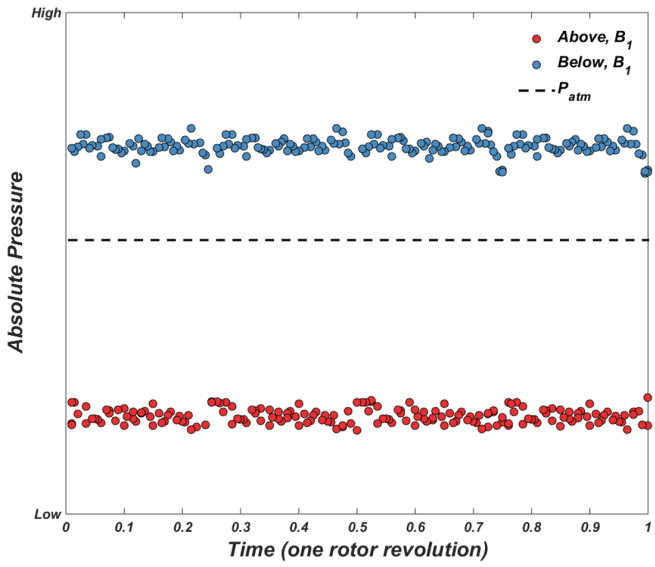

Fig. 14. Time history (one revolution) of HS1 for absolute pressure below and above blade at r/R= 0.85 **(RotUNS unsteady calculations).**

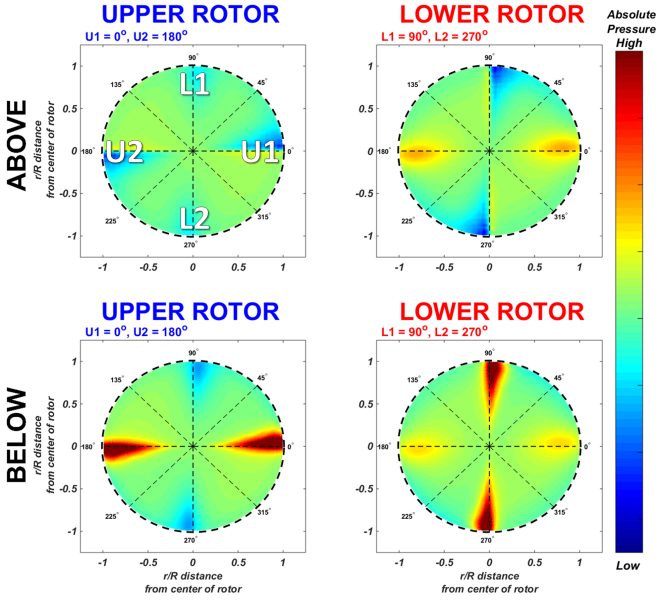

Fig. 15. HC1 comparison of upper and lower rotor of absolute pressure below and above rotor, respectively, at non-overlap (RotUNS unsteady calculations).

CONCLUDING REMARKS

With a future goal to understand aeroacoustics of coaxial rotorcraft, initial steps were taken to investigate the flow field between two counter-rotating rotors while comparing results to an isolated rotor. First, experimental results for the isolated and coaxial Harrington rotors were used to validate the RotUNS rotor disk model calculations for hover and forward flight. For hover, the RotUNS calculations compared well with the experimental data for both the single and coaxial rotor, where BEMT calculations diverged. RotUNS forward

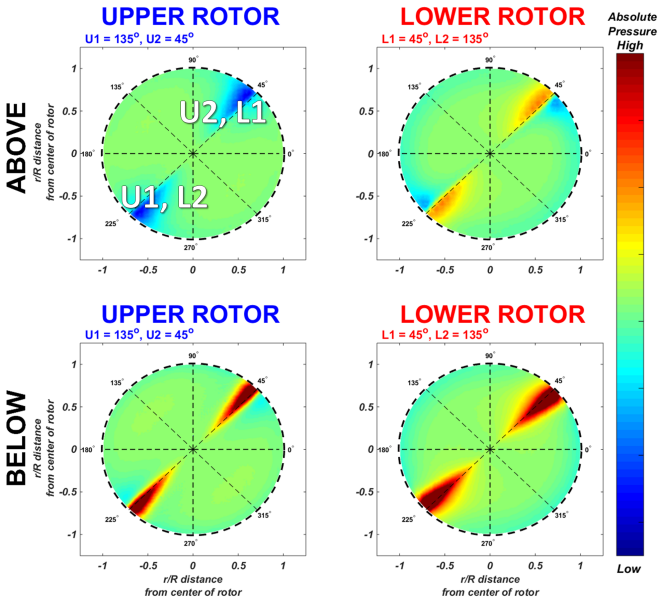

Fig. 16. HC1 comparison of upper and lower rotor of absolute pressure below and above rotor, respectively, at overlap (RotUNS unsteady calculations).

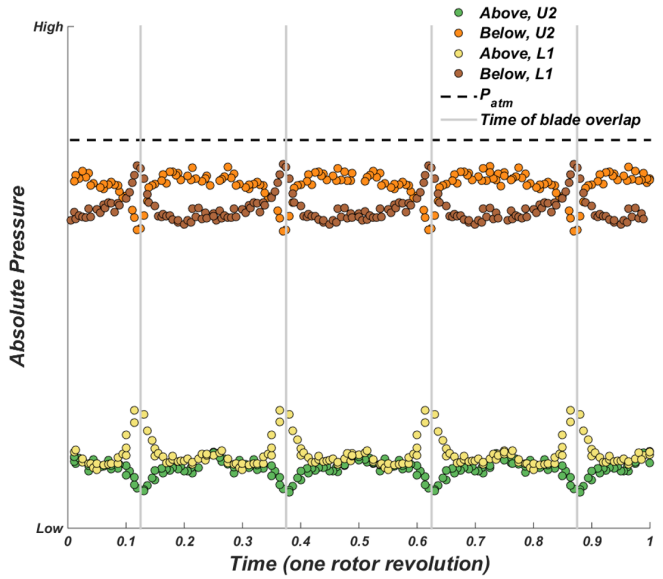

Fig. 17. Time history (one revolution) of HC1 for absolute pressure below and above blade at r/R= 0.85 for upper and lower blades respectively to upper and lower rotor RotUNS unsteady calculations.

flight calculations used trim control solutions calculated from CAMRAD II, which resulted in RotUNS having a larger difference from experimental data compared to CAMRAD II.

An OVERFLOW simulation of two airfoils traveling in opposite directions helped the understanding of pressure field behavior of the RotUNS simulation of a coaxial rotor in hover.

This initial validation of RotUNS and exploration of the complex flow field of coaxial rotors provides a basis for using RotUNS to rapidly study the effect of parametric changes (blade number, blade planform, etc.) on coaxial rotor performance and ultimately, acoustics. RotUNS together with higher-fidelity CFD and acoustic analyses will be used to study noise mitigation of a coaxial rotor system.

With the insights gained from the present work, future work will focus on predicting the acoustics of a coaxial rotor. The end goal is to develop an analysis approach to tailor the aerodynamics and geometry of the two rotors to mitigate noise.

ACKNOWLEDGMENTS

The authors would like to thank the National Aeronautics and Space Administration (NASA) and the U. S. Army Aviation Development Directorate (AFDD), with personal thanks to Dr. William Warmbrodt (NASA), Dr. Gloria Yamauchi (NASA) and Dr. Ben Sim (AFDD) for their support and guidance. Dr. Kenneth Brentner (The Pennsylvania State University) is also acknowledged for his support and advice in the research. We also thank Mr. Mark Potsdam (AFDD) for setting up and running the 2D OVERFLOW calculations and Dr. Wayne Johnson for providing the CAMRAD II trim settings for the forward flight cases.

AUTHORS CONTACT

Natasha Lydia Barbely, Natasha.L.Barbely@nasa.gov; Narayanan M. Komerath, komerath@gatech.edu; Luke Allen Novak, luke.a.novak@sukra-helitek.com

REFERENCES

[1]Mosher, M. and Peterson, R. L., "Acoustic measurements of a full-scale coaxial helicopter," Paper AIAA-83-0722, American Institute of Aeronautics and Astronautics, Aeroacoustics Conference, Atlanta, GA, April 11-13, 1983.

[2]Wachspress, D. A. and Quackenbush, T. R., "Impact of Rotor Design on Coaxial Rotor Performance, Wake Geometry and Noise," American Helicopter Society 62nd Annual Forum, Phoenix, AZ, May 9-11, 2006.

[3]Kim, H. W., Duraisamy, K., and Brown, R. E., "Aeroacoustics of a Coaxial Rotor in Level Flight," American Helicopter Society 64th Annual Forum, Montreal, Canada, April 29 - May 1, 2008.

[4]Kim, H. W., Duraisamy, K., and Brown, R. E., "Effect of Rotor Stiffness and Lift Offset on the Aeroacoustics of a Coaxial Rotor in Level Flight," American Helicopter Society 65th Annual Forum, Grapevine, TX, May 27-29, 2009.

[5]Samokhin, V., Kotlyar, A., and Burtsev, B., "Acoustic Certification of Helicopter Ka-32A," 27th European Rotorcraft Forum, Moscow, Russia, September 2001.

[6]Boyd, D., Burley, C., and Conner, D., "Acoustic Predictions of Manned and Unmanned Rotorcraft Using the Comprehensive Analytical Rotorcraft Model for Acoustics

(CARMA) Code System," American Helicopter Society International Specialists' Meeting on Unmanned Rotorcraft, Chandler, AZ, January 2005.

[7]Coleman, C. P., "A Survey of Theoretical and Experimental Coaxial Rotor Aerodynamic Research," NASA TP- 3675, March 1997.

[8]Taylor, M. K., "A balsa-dust technique for air-flow visualization and its application to flow through model helicopter rotors in static thrust," NACA TN- 2220, November 1950.

[9]Ramasamy, M., "Measurements Comparing Hover Performance of Single, Coaxial, Tandem, and Tilt-Rotor Configurations," American Helicopter Society 69th Annual Forum, Phoenix, AZ, May 21-23, 2013.

[10]Cameron, C. G., Uehara, D., and Sirohi, J., "Transient Hub Loads and Blade Deformation of a Mach-Scale Coaxial Rotor in Hover," Paper AIAA 2015-1412, American Institute of Aeronautics and Astronautics Science and Technology Forum and Exposition, SciTech, Orlando, FL, January 5-9, 2015.

[11]Walsh, D., Weiner, S., Arifian, K., Lawrence, T., Wilson, M., Millott, T., and Blackwell, R., "High Airspeed Testing of the Sikorsky X2 Technology Demonstrator," American Helicopter Society 67th Annual Forum, Virginia Beach, VA, May 3-5, 2011.

[12]Leishman, J. G. and Ananthan, S., "An optimum coaxial rotor system for axial flight," *Journal of the American Helicopter Society*, Vol. 53, (4), 2008, pp. 366–381.

[13]Harrington, R. D., "Full-scale-tunnel investigation of the static-thrust performance of a coaxial helicopter rotor," NACA TN- 2318, March 1951.

[14]Leishman, J. G. and Syal, M., "Figure of Merit Definition for Coaxial Rotors," *Journal of the American Helicopter Society*, Vol. 53, (3), July 2008, pp. 290–300.

[15]Ho, J. C., Yeo, H., and Bhagwat, M., "Validation of Rotorcraft Comprehensive Analysis Performance Predictions for Coaxial Rotors in Hover," American Helicopter Society 71st Annual Forum, Virginia Beach, VA, May 5-7, 2015.

[16]Dingeldein, R. C., "Wind-tunnel studies of the performance of multirotor configurations," NACA TN- 3236, August 1954.

[17]Kim, H. W. and Brown, R. E., "Computational investigation of small scale coaxial rotor aerodynamics in hover," American Helicopter Society 62nd Annual Forum, Phoenix, AZ, May 9-11, 2006.

[18]Kim, H. W. and Brown, R. E., "Coaxial rotor performance and wake dynamics in steady and maneuvering flight," American Helicopter Society 62nd Annual Forum, Phoenix, AZ, May 9-11, 2006.

[19]Juhasz, O., Sya, M., l Roberto Celi, Khromov, V., Rand, O., Ruzicka, G. C., and Strawn, R. C., "Comparison of Three Coaxial Aerodynamic Prediction Methods Including Validation with Model Test Data," *Journal of the American Helicopter Society*, Vol. 59, (4), 2010, pp. 366–381.

[20]Schmaus, J. and Chopra, I., "Aeromechanics for a High Advance Ratio Coaxial Helicopter," American Helicopter Society 71st Annual Forum, Virginia Beach, VA, May 5-7, 2015.

[21]Singh, R. and Kang, H., "Computational Investigations of Transient Loads and Blade Deformations on Coaxial Rotor Systems," Paper AIAA 2015-2884, 33rd American Institute of Aeronautics and Astronautics Applied Aerodynamics Conference, Dallas, TX, June 22-26, 2015.

[22]McAlister, K. W., Tung, C., Rand, O., Khromov, V., and Wilson, J. S., "Experimental and Numerical Study of a Model Coaxial Rotor," American Helicopter Society 62nd Annual Forum, Phoenix, AZ, May 9-11, 2006.

[23]Arents, D. N., "An assessment of the hover performance of the XH-59A advancing blade concept demonstration helicopter," Report USAAMRDL-TN- 25, May 1977.

[24]Rajagopalan, R. G., Baskaran, V., Hollingsworth, A., Lestari, A., Garrick, D., Solis, E., and Hagerty, B., "RotCFD-A Tool for Aerodynamic Interference of Rotors: Validation and Capabilities," American Helicopter Society Aeromechanics Specialists Conference, San Francisco, CA, January 18-20, 2012.

[25]Guntupalli, K., Novak, L. A., and Rajagopalan, R. G., "RotCFD: An Integrated Design Environment for Rotorcraft," American Helicopter Society Aeromechanics Specialists Conference, San Francisco, CA, January 20-22, 2016.

[26]Leishman, J. G., *Principles of Helicopter Aerodynamics*, Cambridge University Press, New York, NY, 2000, Chapter 10.

[27]Johnson, W., *Helicopter Theory*, Princeton University Press, Princeton, NJ, 1980, pp. 808–813.

[28]Johnson, W., "Influence of Lift Offset on Rotorcraft Performance," NASA TP- 215404, November 2009.

[29]Johnson, W., "A Comprehensive Analytical Model of Rotorcraft Aerodynamics and Dynamics, Part I: Analytical Development," NASA TM- 81182, June 1980.

[30]Nichols, R. and Buning, P., "Users Manual for OVERFLOW 2.2," *NASA Langley Research Center, Hampton, VA, Aug*, 2010.

[31]Bertin, J. J. and Smith, M. L., *Aerodynamics for engineers*, Prentice-Hall, 1998, pp. 49–143.

[32]MATLAB, *version 7.10.0 (R2010a)*, The MathWorks Inc., Natick, Massachusetts, 2010.

[33]Nagashima, T. and Nakanishi, K., "Optimum performance and wake geometry of a coaxial rotor in hover," *Vertica*, Vol. 7, 1983, pp. 225–239.

[34]Akimov, A., Butov, V., and Bourtsev, B., "Flight Investigation of Coaxial Rotor Tip Vortex Structure," American Helicopter Society 50th Annual Forum, Washington, D.C., May 1994.

[35]Bagai, A., "Aerodynamic Design of the X2 Technology Demonstrator Main Rotor Blade," American Helicopter Society 64th Annual Forum, Montreal, Canada, April 29 - May 1, 2008.

[36]Ruzicka, G. and Strawn, R., "Computational Fluid Dynamics Analysis of a Coaxial Rotor Using Overset Grids," American Helicopter Society Aeromechanics Specialists Conference, San Francisco, CA, January 23-25, 2008.

[37]Lim, J. W., McAlister, K. W., and Johnson, W., "Hover Performance Correlation for Full-Scale and Model-Scale Coaxial Rotors," American Helicopter Society 63rd Annual Forum, Virginia Beach, VA, May 1-3, 2007.

[38]Ruddell, A., Groth, W., and McCutcheon, R., "Advancing Blade Concept (ABC) Technology Demonstrator," Report USAAVRADCOM-TR-81-D- 5, April 1981.

[39]Bohorquez, F., *Rotor hover performance and system design of an efficient coaxial rotary wing micro air vehicle*, Ph.D. thesis, Department of Aerospace Engineering, University of Maryland, 2007.

[40]Lakshminarayan, V. K. and Baeder, J. D., "Computational investigation of small scale coaxial rotor aerodynamics in hover," Paper AIAA 2009-1069, 47th American Institute of Aeronautics and Astronautics Aerospace Sciences Meeting Including The New Horizons Forum and Aerospace Exposition, Orlando, FL, January 5-8, 2009.

[41]Johnson, W., Moodie, A. M., and Yeo, H., "Design and Performance of Lift-Offset Rotorcraft for Short-Haul Missions," American Helicopter Society Aeromechanics Specialists Conference, San Francisco, CA, January 18-20, 2012.

[42]Yeo, H. and Johnson, W., "Investigation of Maximum Blade Loading Capability of Lift-Offset Rotors," American Helicopter Society 69th Annual Forum, Phoenix, AZ, May 21-23, 2013.

[43]Rajmohan, N., Zhao, J., and He, C., "A Coupled Vortex Particle/CFD Methodology for Studying Coaxial Rotor Configurations," American Helicopter Society Aeromechanics Specialists Conference, San Francisco, CA, January 22-24, 2014.

Table 1. Computational investigations of coaxial rotors in hover and forward flight.

Citation	Flight condition	R(ft)	Tip speed (ft/s)	N_b (per rotor)	σ	Z/D	Data used for validation
Leishman and Ananthan	hover	12.5	500	2	0.054	0.095	Harrington (Ref. 13)
2006 (Ref. 12)	hover	12.5	327, 392	2	0.152	0.080	(Ref. 13)
Wachspress and	hover	1.25	400	4	0.200	0.105-0.5	Nagashima et al. (Ref. 33)
Quackenbush 2006 (Ref. 2)	forward flight	26.0	740	3	0.119	0.095	Kamov Ka-32 (Ref. 34)
McAlister et al.	hover	2.04	165	3	0.014	0.1-0.73	McAlister et al. (Ref. 22)
2006 (Ref. 22)							
Bagai et al.	hover	13.2	620	4	0.660	N/A	Sikorsky X2 (Ref. 11)
2008 (Refs. 11, 35)		13.2	620	4	0.660	N/A	(Ref. 11)
Ruzicka and Strawn	hover	2.04	165	3	0.014	0.1-0.73	(Ref. 22)
2008 (Ref. 36)							
Kim and Brown	hover	12.5	500	2	0.054	0.095	(Ref. 13)
2009 (Refs. 3, 4, 17, 18)	forward flight	12.5	469	2	0.054	0.095	Dingeldein (Ref. 16)
Lim at al.	hover	12.5	500	2	0.054	0.095	(Ref. 13)
2009 (Ref. 37)	hover	12.5	327, 392	2	0.152	0.080	(Ref. 13)
	hover	2.04	165	3	0.014	0.1-0.73	(Ref. 22)
	hover	18.0	650	3	0.127	0.0694	XH-59A (Ref. 23)
Johnson	hover	18.0	650	3	0.127	0.0694	(Ref. 23)
2009 (Ref. 28)	hover	12.5	500	2	0.054	0.095	(Ref. 13)
	hover	12.5	327, 392	2	0.152	0.080	(Ref. 13)
	forward flight	18.0	650	3	0.127	0.0694	(Refs. 23, 38)
	forward flight	12.5	469	2	0.054	0.095	(Ref. 16)
Lakshminarayan	hover	12.5	327, 392	2	0.152	0.080	(Ref. 13)
and Baeder	hover	0.28	55-80	3	0.128	0.625	Bohorquez (Ref. 39)
2009 (Ref. 40)							
Juhasz et al.	hover	12.5	500	2	0.054	0.095	(Ref. 13)
2010 (Refs. 19, 20)	hover	2.04	165	3	0.014	0.1-0.73	(Ref. 22)
	forward flight	18.0	650	3	0.127	0.0694	(Ref. 23)
	forward flight	2.04	165	3	0.014	0.1-0.73	(Ref. 22)
Johnson et al.	hover	18.0	650	3	0.127	0.0694	(Ref. 23)
2012 (Ref. 41)	hover	13.2	620	4	0.660	N/A	(Ref. 11)
	forward flight	18.0	650	3	0.127	0.0694	(Ref. 23)
	forward flight	13.2	620	4	0.660	N/A	(Ref. 11)
Yeo et al.	hover	18.0	650	3	0.127	0.0694	(Ref. 23)
2013 (Ref. 42)	forward flight	18.0	650	3	0.127	0.0694	(Ref. 23)
Rajmohan et al.	hover	2.04	165	3	0.014	0.1-0.73	(Ref. 22)
2014 (Ref. 43)							
Ho et al.	hover	12.5	500	2	0.054	0.095	(Ref. 13)
2015 (Ref. 15)	hover	12.5	327, 392	2	0.152	0.080	(Ref. 13)
	hover	2.17	182, 273	3	0.168	0.05-1.5	Ramasamy (Ref. 9)
	hover	2.15	180, 270	3	0.148	0.05-0.75	(Ref. 9)
Schmaus and Chopra	hover	12.5	500	2	0.054	0.095	(Ref. 13)
2015 (Ref. 20)	hover	18.0	650	3	0.127	0.0694	(Ref. 23)
	hover	3.83	573	2	0.153	0.060	University of Texas (Ref. 10)
Singh and Kang	hover	12.5	500	2	0.054	0.095	(Ref. 13)
2015 (Ref. 21)	hover	3.83	573	2	0.153	0.060	(Ref. 10)
Barbely et al.	hover	12.5	500	2	0.054	0.095	(Ref. 13)
2016	forward flight	12.5	469	2	0.054	0.095	(Ref. 16)

Table 2. HS1/HC1 parameters (Ref. 13).

Parameter	Harrington rotor 1
Radius (ft)	12.5
No. of blades (per rotor)	2
Chord (ft)	varying
Z, rotor separation (ft)	2.33
Tip speed, hover (ft/sec)	500
Tip speed, forward flight (ft/sec)	469
Solidity	0.054
Solidity per rotor	0.027
Twist	None
Taper	linear distribution
Airfoils (thickness ratio)	non-linear distribution
Cutout radius (r/R)	0.133
Hinge offset (r/R)	0.133
Upper rotor direction (HS1/HC1)	Clockwise
Lower rotor direction (HC1)	Counter-Clockwise

Table 3. HC1 hover RotUNS steady control inputs(* with grid adaptions (GA)).

θ_U (deg)	θ_L (deg)	% diff in Q
1.5	1.5	0.28
1.5*	1.5*	0.56
3.0	3.2	0.45
5.0	5.2	0.75
5.0*	5.0*	3.28
7.0	7.2	0.19
8.0	8.2	0.19
8.0*	8.0*	2.21
9.0	9.2	0.57
10.0	10.2	0.95
10.0*	10.0*	1.27
11.0	11.0	0.38
11.9	12.0	0.91
12.0*	12.0*	0.18

Table 4. HC1 hover RotUNS steady control inputs for varying separation distance

Z/D	θ_U (deg)	θ_L (deg)	% diff in Q
0.050	7.0	7.0	1.79
0.093	7.0	7.0	1.77
0.125	7.0	7.2	0.65
0.250	7.0	7.25	0.89
0.500	7.0	7.2	1.86
1.000	7.0	7.10	1.48
1.500	7.0	7.10	0.81

Table 5. HC1 forward flight RotUNS inputs using CAMRAD II control settings (Ref. 28).

μ	0.12	0.16	0.18	0.20	0.22	0.24
α_S (deg)	-2.16	-3.64	-4.51	-5.47	-6.46	-7.53
Lower rotor						
θ_L (deg)	7.98	8.27	8.67	9.19	9.85	10.65
$\theta_1 s$ (deg)	-2.43	-3.35	-3.85	-4.36	-5.07	-5.75
$\theta_1 c$ (deg)	1.32	0.81	0.69	0.63	0.55	0.5
Upper Rotor						
θ_U (deg)	8.07	8.31	8.69	9.21	9.87	10.68
$\theta_1 s$(deg)	-2.75	-3.55	-4.03	-4.57	-5.19	-5.9
$\theta_1 c$(deg)	1.05	0.69	0.59	0.5	0.42	0.36

Table 6. HC1 forward flight RotUNS steady control inputs

μ	θ_U (deg)	θ_L (deg)	% diff in Q
0.12	7.98	8.07	0.47
0.16	8.27	8.31	0.15
0.18	8.67	8.69	0.15
0.20	9.19	9.21	0.05
0.22	9.85	9.87	0.16
0.24	10.65	10.68	0.17